Transducer-Plane Streaming Patterns in Thin-Layer Acoustofluidic Devices

Junjun Lei,* Martyn Hill,† and Peter Glynne-Jones‡
Faculty of Engineering and the Environment, University of Southampton, Southampton SO17 1BJ, United Kingdom
(Received 6 January 2017; revised manuscript received 2 June 2017; published 20 July 2017)

While classical Rayleigh streaming, whose circulations are perpendicular to the transducer radiating surfaces, is well known, transducer-plane streaming patterns, in which vortices circulate parallel to the surface driving the streaming, have been less widely discussed. Previously, a four-quadrant transducer-plane streaming pattern has been seen experimentally and subsequently investigated through numerical modeling. In this paper, we show that by considering higher-order three-dimensional cavity modes of rectangular channels in thin-layer acoustofluidic manipulation devices, a wider family of transducer-plane streaming patterns are found. As an example, we present a transducer-plane streaming pattern, which consists of eight streaming vortices with each occupying one octant of the plane parallel to the transducer radiating surfaces, which we call here eight-octant transducer-plane streaming. An idealized modal model is also presented to highlight and explore the conditions required to produce rotational patterns. We find that both standing and traveling wave components are typically necessary for the formation of transducer-plane streaming patterns. In addition, other streaming patterns related to acoustic vortices and systems in which traveling waves dominate are explored with implications for potential applications.

DOI: 10.1103/PhysRevApplied.8.014018

I. INTRODUCTION

Acoustic streaming is steady fluid motion driven by the absorption of acoustic energy due to the interaction of acoustic waves with the fluid medium or its solid boundaries. Understanding the driving mechanisms of acoustic streaming patterns within acoustofluidic devices is important in order to precisely control it for the enhancement or suppression of acoustic streaming for applications such as particle and cell manipulation [1–8], heat-transfer enhancement [9–12], noncontact surface cleaning [13–17], microfluidic mixing [18–27], and transport enhancement [28–35].

In most bulk microacoustofluidic particle and cell manipulation systems of interest, the acoustic streaming fields are dominated by boundary-driven streaming [36], which is associated with acoustic dissipation in the viscous boundary layer [37]. Theoretical work on boundary-driven streaming was initiated by Rayleigh [38] and developed by a series of modifications for particular cases [39–44], which have paved the fundamental understanding of acoustic streaming flows.

While Rayleigh streaming patterns (which have streaming vortices with components perpendicular to the driving boundaries) have been extensively studied [45–48], we have recently explored the mechanisms behind four-quadrant transducer-plane streaming [49], which generates streaming vortices in planes parallel to the driving boundary, and modal Rayleigh-like streaming [50] in which vortices have a roll size greater than the quarter wavelength of the main acoustic resonance and are driven by *limiting velocities* (the value of the streaming velocity just outside the boundary layer [41,49]), on the boundaries perpendicular to the axis of the main acoustic resonance. The expressions for the limiting velocities have terms corresponding to acoustic velocity gradients along each coordinate axis. Depending on which of these gradients is dominant, different acoustic streaming patterns arise in thin-layer acoustofluidic devices [50], corresponding to the rotational and irrotational features of, respectively, the active and reactive intensity patterns in acoustic fields [51]. The defining feature of transducer-plane streaming is that its vorticity is driven by vorticity in the limiting velocity patterns themselves.

In this paper, we first investigate higher-order transducer-plane streaming patterns in thin-layer acoustofluidic manipulation devices. "Thin-layer" devices are defined here as resonators in which the thickness of the fluid layer (in the direction of the acoustic axis) is less that 1/20th of its lateral dimensions [50] and of the order of half an acoustic wavelength. We introduce a boundary-driven streaming pattern observed in a thin-layer glass capillary device and then investigate the underlying physics of transducer-plane streaming with an analytical model in order to gain insights into the contributions of standing and traveling wave components, respectively.

II. EIGHT-OCTANT TRANSDUCER-PLANE STREAMING

The experiments are performed in a transducer-capillary device using a microparticle-image-velocimetery (μpiv) system as shown in Fig. 1(a), similar to those we used previously [49,50] (see Ref. [52] and details in the

*andyleiapply@gmail.com
†m.hill@soton.ac.uk
‡p.glynne-jones@soton.ac.uk

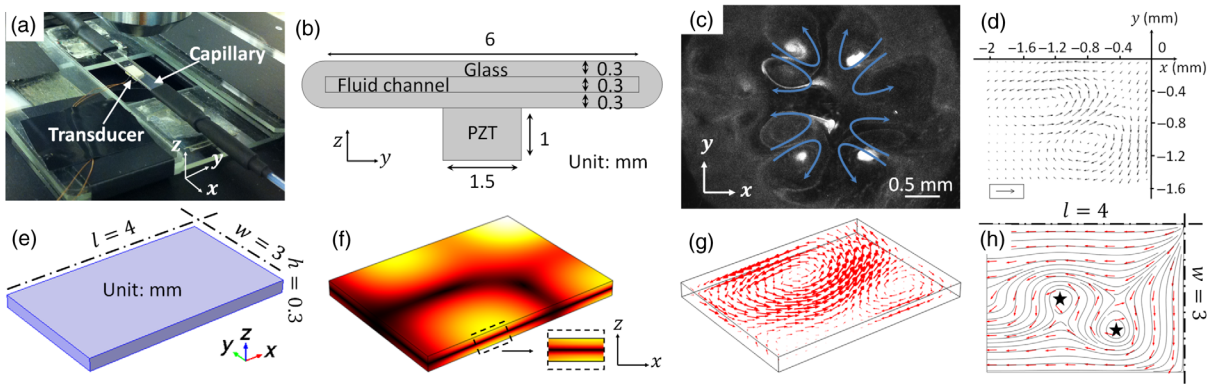

FIG. 1. (a) The experimental acoustofluidic particle manipulation device, where, to connect the capillary to plastic tubing, heat-shrinkable tubing (black) is used at the two ends of the capillary. (b) Cross section of the device. (c) A photographic image of the distribution of beads (radius of 1 μm) in the fluid after some minutes of streaming, where a main eight-octant transducer-plane streaming pattern can be seen in which beads have agglomerated near the center of the streaming vortices and at the center of the device. (d) μpiv measurements of the eight-octant transducer-plane streaming field in the third quadrant shown in (c) at a peak-to-peak voltage of 30 V p.p., where the arrow in the box shows a reference velocity of 20 μm/s. (e) The considered 3D model ($4 \times 3 \times 0.3$ mm^3), where the dashed-dot lines show the symmetry planes. (f) The first-order acoustic pressure field on all surfaces. (g) The 3D acoustic streaming velocity field, where velocity vectors are shown at two heights within the chamber (z positions of one-third and two-thirds of the chamber height). (h) The active intensity (i.e., the limiting velocity field) on the driving boundaries ($z = \pm h/2$), where the five-pointed stars show the points of minimum pressure amplitude, and normalized arrows are used to show the flow directions.

Supplemental Material [53]). This acoustofluidic system is of interest, as it is used elsewhere in a blood and bacterial capture device [1,2]. The measurements are performed within x-y horizontal planes [see Fig. 1(a)]. The investigation area is above the transducer radiating surface. Figure 1(c) shows the streaming pattern observed (at a frequency of 2.498 MHz), where an *eight-octant*, steady acoustic streaming pattern in which each vortex occupies approximately one octant of the viewed x-y horizontal plane. The plane of these vortices is parallel to the transducer radiating surface (i.e., perpendicular to the axis of the main standing wave in the z direction), as is the case for the four-quadrant transducer-plane streaming we have presented previously [49] but in a different plane to the vortices observed in Rayleigh streaming [38]. Detailed fluid motion can be seen in Fig. 1(d), where μpiv results of the streaming field in the third quadrant are presented. It can be seen that vortices are generated, each of which occupies one octant.

To understand the driving mechanism of this eight-octant transducer-plane streaming pattern, the finite-element package COMSOL [54] is used to model the acoustic and streaming fields in the experimental device. In this work, we apply the limiting velocity method [41] based on the perturbation method [44] to model the 3D outer-streaming fields in the capillary device. We have previously established the viability of this method for solving 3D boundary-driven streaming fields in thin-layer acoustofluidic manipulation devices [48–50] and in vibrating-plate systems [55].

III. NUMERICAL MODEL

The full numerical procedure can be split into three steps. First, the first-order acoustic fields within the devices are modeled using the COMSOL "Pressure Acoustics, Frequency Domain" interface, which solves the harmonic, linearized acoustic problems, taking the form:

$$\nabla^2 p_1 = -\frac{\omega^2}{c^2} p_1, \tag{1}$$

where p_1 is the complex acoustic pressure, ω is the angular frequency, and c is the sound speed in the fluid. As the device is symmetric to the center, only a quarter of the fluid channel is modeled here for numerical efficiency, and the model is located within coordinates $-l \le x \le 0$, $-w \le y \le 0$, and $-h/2 \le z \le h/2$ [see Fig. 1(e)]. Edges $x = 0$ and $y = 0$ are set as symmetric boundary conditions. We excite the standing wave field through a "normal acceleration" boundary condition on the bottom surface, as published previously [49,50]. Surface $x = -l$ is set as a plane-wave radiation condition in order to simulate the loss of acoustic energy at the two ends of the fluid channel. The remaining walls are modeled using sound-reflecting boundary conditions, as these are water-glass interfaces and we are working at frequencies away from resonances of these walls.

Second, the limiting velocities at all boundaries are calculated as a function of the first-order acoustic velocity fields. On planar surfaces normal to z, the limiting velocity equations on the driving boundaries ($z = \pm h/2$) take the form [49]

$$u_L = \frac{-1}{4\omega} \mathrm{Re}\left\{ q_x + u_1^* \left[(2+i)\nabla \cdot \boldsymbol{u}_1 - (2+3i)\frac{dw_1}{dz} \right] \right\}, \tag{2a}$$

$$v_L = \frac{-1}{4\omega}\mathrm{Re}\left\{q_y + v_1^*\left[(2+i)\nabla\cdot\boldsymbol{u}_1 - (2+3i)\frac{dw_1}{dz}\right]\right\}, \tag{2b}$$

$$q_x = u_1\frac{du_1^*}{dx} + v_1\frac{du_1^*}{dy}, \tag{2c}$$

$$q_y = u_1\frac{dv_1^*}{dx} + v_1\frac{dv_1^*}{dy}, \tag{2d}$$

where u_L and v_L are the two components of limiting velocities along coordinates x and y, Re{} represents the real part of a complex value, and u_1, v_1, and w_1 are components of the complex first-order acoustic velocity vector $\boldsymbol{u}_1$ along the coordinates x, y, and z, respectively. The superscript * represents the complex conjugate.

Finally, this limiting velocity method is used to model the acoustic streaming fields in this thin-layer acoustofluidic device using the COMSOL "Creeping Flow" interface. Outside of the acoustic boundary layer, the governing equations for the second-order streaming velocities $\boldsymbol{u}_2$ and the associated pressure fields p_2 are

$$\nabla p_2 = \mu\nabla^2\boldsymbol{u}_2, \tag{3a}$$

$$\nabla\cdot\boldsymbol{u}_2 = 0, \tag{3b}$$

where μ is the dynamic viscosity of the fluid. Here, the bottom and top surfaces ($z = \pm h/2$) are considered as limiting velocity boundary conditions, surfaces $x = 0$ and $y = 0$ are symmetric conditions, and the remaining surfaces are no-slip boundary conditions.

The modeled acoustic pressure and acoustic streaming fields at the resonant frequency $f_r = 2.4973$ MHz (obtained from a frequency sweep to find the frequency which gives the maximum energy density in the cavity) in the 3D fluid volumes are shown in Figs. 1(f) and 1(g). It can be seen from Fig. 1(g) that this quadrant model contains two dominant streaming vortices with circulations parallel to the bottom surface (i.e., the transducer radiating surface), which compares well with the measured acoustic streaming vortices shown in Fig. 1(d).

The acoustic pressure field is shown in Fig. 1(f), a mode with a half wavelength in the z direction of the model. The fields along the x and y axes have approximately one-and-a-half- and one-wavelength variations, respectively. The rotational components of transducer-plane streaming are closely linked to the active intensity field [49], which tends to circulate about pressure nodal points [51,56]. The modeled active intensity field in this case is shown in Fig. 1(h) and is consistent with this flow pattern, showing rotation at the boundary about the two regions of minimum pressure amplitude on the surface. These vortices drive the eight-octant transducer-plane streaming patterns in the x-y horizontal planes of the 3D fluid channels, with this higher-order resonance producing a higher-order eight-octant vortex pattern in the active sound intensity field in comparison with four-quadrant streaming.

IV. ANALYTICAL MODEL

We have previously presented results for transducer-plane streaming in acoustofluidic devices [50], showing that rotation in the active intensity is closely linked to the rotational patterns seen in experiments. What was not made clear previously was that a single standing wave mode does not exhibit this rotation of active intensity. To achieve rotational active intensity in a two-dimensional sound field, it is typically necessary to have a line or point pressure minimum [56–58] which can result from the superposition of a traveling and standing wave (see below) or of two standing waves. This observation is supported by our previous models [48–50], where we find that if the radiation boundary conditions (which allowed for the passage of energy across them but still reflected a proportion of that energy to create combinations of standing and traveling waves) are replaced with rigid- or free-boundary conditions, the rotational patterns vanish. Hence, in this section we create an analytical model to study the streaming patterns resulting from simple combinations of cavity modes and traveling modes for a case that generates the four-quadrant transducer-plane streaming patterns in order to obtain more insight into the relative significance of the traveling and standing wave components and the effects of different modes and phase relationships.

In our model, the first-order acoustic pressure field p_1 established in the fluid channel is decomposed into two components, a standing wave component p_{1s} and a traveling wave component (in the x direction) p_{1t},

$$p_1 = p_{1s} + p_{1t}, \tag{4a}$$

$$p_{1s} = p_{0s}\cos(k_{xs}x)\cos(k_{ys}y)\sin(k_{zs}z)e^{i\omega t}, \tag{4b}$$

$$p_{1t} = p_{0t}e^{ik_{xt}x}\cos(k_{yt}y)\sin(k_{zt}z)e^{i(\omega t+\varphi)}, \tag{4c}$$

where subscripts s and t indicate the standing and traveling wave components, respectively, p_0 is the acoustic pressure amplitude, ω is the angular frequency, and φ indicates the phase difference between the standing and traveling wave components. The wave numbers in the x, y, and z directions are k_x, k_y, and k_z. Each wave number has both a standing and traveling wave component, as indicated by the second s or t subscripts.

As we discuss above, the standing (cavity) mode components of Eqs. (4) alone produce irrotational limiting velocity fields, but the combination of traveling and standing wave components is the probable cause of the patterns seen, as borne out by the correspondence between the modeled and experimental results. An example of the

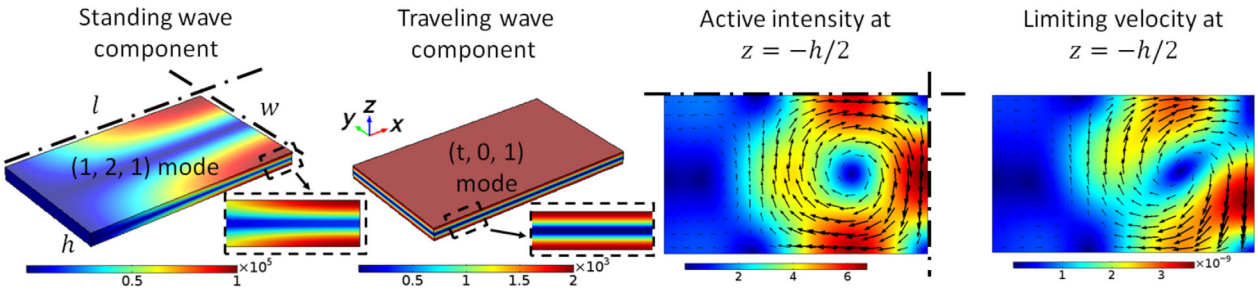

FIG. 2. The active intensity (W/m^2) and limiting velocity (m/s) fields at the driving boundaries for a combination of standing and traveling wave components (Pa). The phase difference between the standing and traveling wave components $\varphi = -\pi/2$. The relationships between the four-quadrant transducer-plane streaming magnitudes, $|\boldsymbol{u}_2|$, the active intensity magnitudes $|\boldsymbol{I}|$, and the acoustic pressure amplitudes are shown in Eq. (5). Arrows in (c) and (d) show the corresponding vector fields.

streaming field created by an acoustic vortex formed from the superposition of two standing wave modes is shown in Fig. S2 in the Supplemental Material [53]. It is interesting to note the applicability of the limiting velocity method in this case.

Here we take the four-quadrant streaming pattern as an example (perhaps the simplest) to illustrate the roles of, respectively, the standing and traveling wave components [50]. The limiting velocity fields at the driving boundaries for various combinations of standing and traveling wave components are examined. We find that the regular four-quadrant vortex pattern is obtained for a combination of the (1, 2, 1) standing wave mode and $(t, 0, 1)$ traveling wave mode shown in Fig. 2.

The corresponding patterns with other traveling wave components can be found in the Supplemental Material [53]. In a real device, combinations of these modes might be excited, and it is interesting to note that the traveling wave modes $(t, n, 0)$ do not produce transducer-plane streaming, and the higher-order mode $(t, 1, 1)$ can produce rotation in the opposite direction. Real devices will exhibit complex patterns and mode combinations that are less

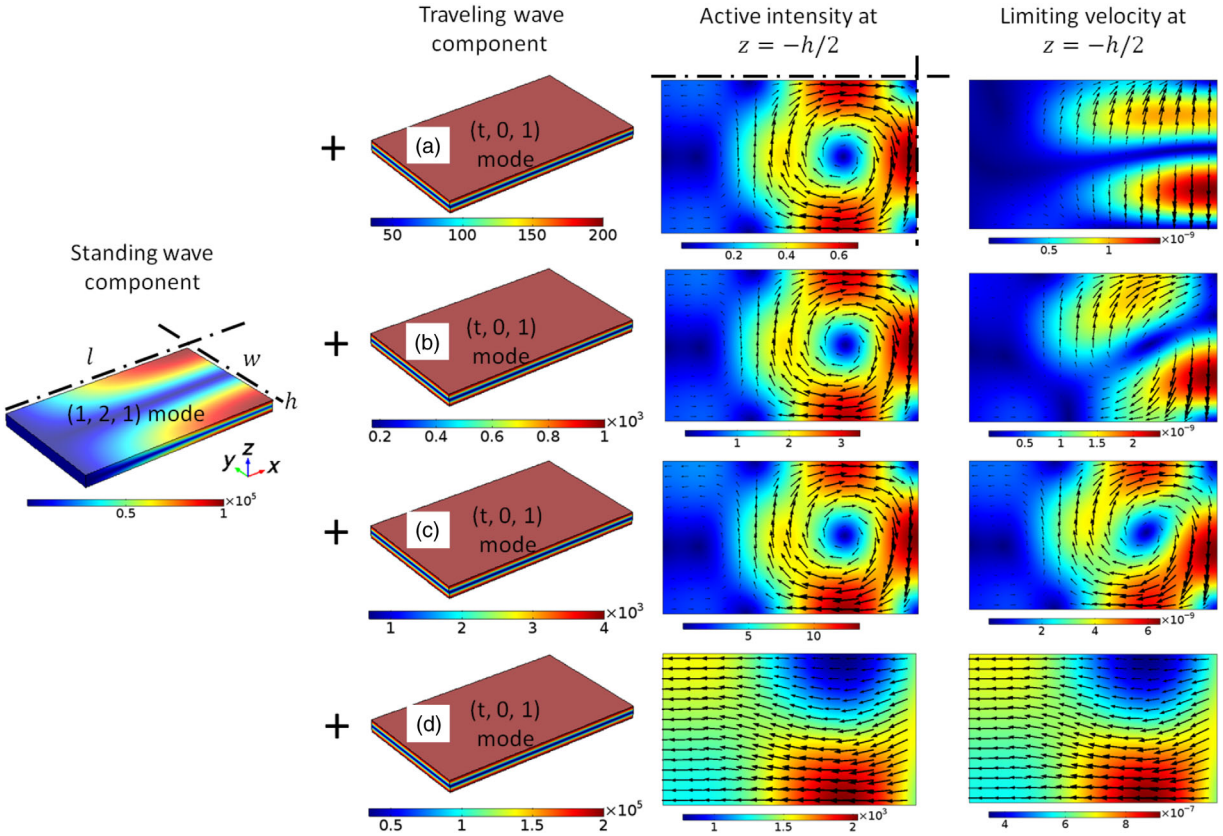

FIG. 3. The active intensity (W/m^2) and limiting velocity (m/s) fields at the driving boundaries for a number of standing and traveling wave components (Pa). The phase difference between the standing and traveling wave components $\varphi = -\pi/2$.

idealized than those presented here, but we suspect that the higher-order modes are less likely to be exhibited in experimental devices.

Figure 3 shows the transitions of streaming patterns from various ratios of standing and traveling wave pressure amplitudes. For very small values of p_{0t}, modal Rayleigh-like streaming patterns [50] are seen [Fig. 3(a)]. As p_{0t} increases, a gradual transition to the transducer-plane pattern is seen [Figs. 3(b) and 3(c)]. Ultimately, as p_{0t} approaches p_{0s}, irrotational terms become more dominant, leading to limiting velocities which follow the predominantly x-directed active intensity of the traveling wave [Fig. 3(d)], which will drive flow if the end boundaries allow for the passage of fluid.

For this specific mode, the limiting velocity (and, hence, the magnitude of the transducer-plane streaming vortices) is found to be approximately proportional (to within 5%) to that of the active intensity following (see derivation in the Supplemental Material [53])

$$|I|_{\max} \approx \frac{k_{xt} p_{0t}^2}{2\rho_0 \omega}\left(1 + \frac{p_{0s}}{p_{0t}}\right). \tag{5}$$

For $p_{0t} < p_{0s}$, increasing p_{0t} shifts the vortex center outwards in the y direction, while much larger values create a pattern resembling the uniform active intensity which follows the direction of propagation of the now dominant traveling wave component. We also find that introducing a phase difference between the standing and traveling wave components φ shifts the vortex in the x direction.

We also note that the model shows that in situations where the traveling wave component is dominant, the limiting velocity at the boundary is nonzero. This limiting velocity will drive a streaming pattern in addition to the (typically higher velocity) Eckart streaming which will also be present in these cases. Combinations of traveling waves in the x direction with standing modes in z (or a pure traveling wave field) reveal that the limiting velocity can take the opposite direction to Eckart streaming in these cases, leading to streaming vortices near the boundaries (see Fig. S3 in the Supplemental Material [53]), as has been seen in a surface acoustic wave device where the thickness of the fluid is at or less than the viscous penetration depth [59].

V. CONCLUSION

In conclusion, we demonstrate that a wider range of transducer-plane streaming patterns exist other than the four-quadrant pattern that had been observed previously related to higher-order cavity modes. As an example, we predict numerically an eight-octant transducer-plane streaming, and we find it experimentally in a glass capillary device. We create a simplified analytical model to provide deeper insight into the underlying physics of transducer-plane streaming patterns in thin-layer acoustofluidic devices. The model highlights the importance of having both standing and (typically smaller) traveling wave components present within the acoustic cavity to create rotational motion in the limiting velocity and resulting streaming fields. We show that the limiting velocity method also predicts the rotational streaming found from other acoustic vortices. The model also highlights how fields with stronger traveling wave components also exhibit boundary-driven streaming creating limiting velocities at the boundaries which are not found from pure Eckart streaming, and that interactions between boundary-driven streaming and Eckart streaming can create inner streaming vortices.

The models used to generate the simulation data and experimental data supporting this study are openly available from the University of Southampton repository at [60].

ACKNOWLEDGMENTS

This work is supported by the EPSRC/University of Southampton Doctoral Prize Fellowship No. EP/N509747/1. P. G. J. also acknowledges support from EPSRC Fellowship No. EP/L025035/1.

[1] B. Hammarstrom, T. Laurell, and J. Nilsson, Seed particle-enabled acoustic trapping of bacteria and nanoparticles in continuous flow systems, Lab Chip **12**, 4296 (2012).
[2] B. Hammarstrom, B. Nilson, T. Laurell, J. Nilsson, and S. Ekstrom, Acoustic trapping for bacteria identification in positive blood cultures with MALDI-TOF MS, Anal. Chem. **86**, 10560 (2014).
[3] S. K. Chung and S. K. Cho, On-chip manipulation of objects using mobile oscillating bubbles, J. Micromech. Microeng. **18**, 125024 (2008).
[4] B. R. Lutz, J. Chen, and D. T. Schwartz, Hydrodynamic tweezers: 1. Noncontact trapping of single cells using steady streaming microeddies, Anal. Chem. **78**, 5429 (2006).
[5] S. Yazdi and A. M. Ardekani, Bacterial aggregation and biofilm formation in a vortical flow, Biomicrofluidics **6**, 044114 (2012).
[6] M. Antfolk, P. B. Muller, P. Augustsson, H. Bruus, and T. Laurell, Focusing of sub-micrometer particles and bacteria enabled by two-dimensional acoustophoresis, Lab Chip **14**, 2791 (2014).
[7] C. Wang, S. V. Jalikop, and S. Hilgenfeldt, Size-sensitive sorting of microparticles through control of flow geometry, Appl. Phys. Lett. **99**, 034101 (2011).
[8] C. Devendran, I. Gralinski, and A. Neild, Separation of particles using acoustic streaming and radiation forces in an open microfluidic channel, Microfluid. Nanofluid. **17**, 879 (2014).
[9] M. Nabavi, K. Siddiqui, and J. Dargahi, Effects of transverse temperature gradient on acoustic and streaming velocity fields in a resonant cavity, Appl. Phys. Lett. **93**, 051902 (2008).
[10] B. G. Loh, S. Hyun, P. I. Ro, and C. Kleinstreuer, Acoustic streaming induced by ultrasonic flexural vibrations and associated enhancement of convective heat transfer, J. Acoust. Soc. Am. **111**, 875 (2002).

[11] S. Hyun, D. R. Lee, and B. G. Loh, Investigation of convective heat transfer augmentation using acoustic streaming generated by ultrasonic vibrations, Int. J. Heat Mass Transfer **48**, 703 (2005).
[12] M. K. Aktas, B. Farouk, and Y. Q. Lin, Heat transfer enhancement by acoustic streaming in an enclosure, J. Heat Transfer **127**, 1313 (2005).
[13] W. Kim, T. H. Kim, J. Choi, and H. Y. Kim, Mechanism of particle removal by megasonic waves, Appl. Phys. Lett. **94**, 081908 (2009).
[14] E. Maisonhaute, C. Prado, P. C. White, and R. G. Compton, Surface acoustic cavitation understood via nanosecond electrochemistry. Part III: Shear stress in ultrasonic cleaning, Ultrason. Sonochem. **9**, 297 (2002).
[15] S. K. R. S. Sankaranarayanan, S. Cular, V. R. Bhethanabotla, and B. Joseph, Flow induced by acoustic streaming on surface-acoustic-wave devices and its application in biofouling removal: A computational study and comparisons to experiment, Phys. Rev. E **77**, 066308 (2008).
[16] A. A. Busnaina, I. I. Kashkoush, and G. W. Gale, An experimental study of megasonic cleaning of silicon wafers, J. Electrochem. Soc. **142**, 2812 (1995).
[17] M. Keswani, S. Raghavan, P. Deymier, and S. Verhaverbeke, Megasonic cleaning of wafers in electrolyte solutions: Possible role of electro-acoustic and cavitation effects, Microelectron. Eng. **86**, 132 (2009).
[18] D. Ahmed, X. L. Mao, J. J. Shi, B. K. Juluri, and T. J. Huang, A millisecond micromixer via single-bubble-based acoustic streaming, Lab Chip **9**, 2738 (2009).
[19] K. Sritharan, C. J. Strobl, M. F. Schneider, A. Wixforth, and Z. Guttenberg, Acoustic mixing at low Reynold's numbers, Appl. Phys. Lett. **88**, 054102 (2006).
[20] R. Shilton, M. K. Tan, L. Y. Yeo, and J. R. Friend, Particle concentration and mixing in microdrops driven by focused surface acoustic waves, J. Appl. Phys. **104**, 014910 (2008).
[21] T. D. Luong, V. N. Phan, and N. T. Nguyen, High-throughput micromixers based on acoustic streaming induced by surface acoustic wave, Microfluid. Nanofluid. **10**, 619 (2011).
[22] T. Frommelt, M. Kostur, M. Wenzel-Schafer, P. Talkner, P. Hanggi, and A. Wixforth, Microfluidic Mixing Via Acoustically Driven Chaotic Advection, Phys. Rev. Lett. **100**, 034502 (2008).
[23] R. H. Liu, J. N. Yang, M. Z. Pindera, M. Athavale, and P. Grodzinski, Bubble-induced acoustic micromixing, Lab Chip **2**, 151 (2002).
[24] G. G. Yaralioglu, I. O. Wygant, T. C. Marentis, and B. T. Khuri-Yakub, Ultrasonic mixing in microfluidic channels using integrated transducers, Anal. Chem. **76**, 3694 (2004).
[25] M. K. Tan, L. Y. Yeo, and J. R. Friend, Rapid fluid flow and mixing induced in microchannels using surface acoustic waves, Europhys. Lett. **87**, 47003 (2009).
[26] D. Ahmed, X. L. Mao, B. K. Juluri, and T. J. Huang, A fast microfluidic mixer based on acoustically driven sidewall-trapped microbubbles, Microfluid. Nanofluid. **7**, 727 (2009).
[27] C. Suri, K. Takenaka, Y. Kojima, and K. Koyama, Experimental study of a new liquid mixing method using acoustic streaming, J. Chem. Eng. Jpn. **35**, 497 (2002).
[28] B. Moudjed, V. Botton, D. Henry, S. Millet, J. P. Garandet, and H. Ben Hadid, Oscillating acoustic streaming jet, Appl. Phys. Lett. **105**, 184102 (2014).
[29] R. H. Nilson and S. K. Griffiths, Enhanced transport by acoustic streaming in deep trench-like cavities, J. Electrochem. Soc. **149**, G286 (2002).
[30] T. Maturos *et al.*, Enhancement of DNA hybridization under acoustic streaming with three-piezoelectric-transducer system, Lab Chip **12**, 133 (2012).
[31] P.-H. Huang, N. Nama, Z. Mao, P. Li, J. Rufo, Y. Chen, Y. Xie, C.-H. Wei, L. Wang, and T. J. Huang, A reliable and programmable acoustofluidic pump powered by oscillating sharp-edge structures, Lab Chip **14**, 4319 (2014).
[32] D. Moller, T. Hilsdorf, J. T. Wang, and J. Dual, Acoustic streaming used to move particles in a circular flow in a plastic chamber, AIP Conf. Proc. **1433**, 775 (2012).
[33] R. M. Moroney, R. M. White, and R. T. Howe, Microtransport induced by ultrasonic Lamb waves, Appl. Phys. Lett. **59**, 774 (1991).
[34] N. Li, J. H. Hu, H. Q. Li, S. Bhuyan, and Y. J. Zhou, Mobile acoustic streaming based trapping and 3-dimensional transfer of a single nanowire, Appl. Phys. Lett. **101**, 093113 (2012).
[35] M. Miansari and J. R. Friend, Acoustic nanofluidics via room-temperature lithium niobate bonding: A platform for actuation and manipulation of nanoconfined fluids and particles, Adv. Funct. Mater. **26**, 7861 (2016).
[36] M. Wiklund, R. Green, and M. Ohlin, Acoustofluidics 14: Applications of acoustic streaming in microfluidic devices, Lab Chip **12**, 2438 (2012).
[37] H. Bruus, Acoustofluidics 10: Scaling laws in acoustophoresis, Lab Chip **12**, 1578 (2012).
[38] Lord Rayleigh, On the circulation of air observed in Kundt's tube, and on some allied acoustical problems, Phil. Trans. R. Soc. London **175**, 1 (1884).
[39] H. Schlichting, Berechnung ebener periodischer Grenzschichtströmungen (Calculation of plane periodic boundary layer streaming), Phys. Z. **33**, 327 (1932).
[40] P. J. Westervelt, The theory of steady rotational flow generated by a sound field, J. Acoust. Soc. Am. **25**, 60 (1953).
[41] W. L. Nyborg, Acoustic streaming near a boundary, J. Acoust. Soc. Am. **30**, 329 (1958).
[42] J. Lighthill, Acoustic streaming, J. Sound Vib. **61**, 391 (1978).
[43] M. F. Hamilton, Y. A. Ilinskii, and E. A. Zabolotskaya, Acoustic streaming generated by standing waves in two-dimensional channels of arbitrary width, J. Acoust. Soc. Am. **113**, 153 (2003).
[44] S. S. Sadhal, Acoustofluidics 13: Analysis of acoustic streaming by perturbation methods Foreword, Lab Chip **12**, 2292 (2012).
[45] M. K. Aktas and B. Farouk, Numerical simulation of acoustic streaming generated by finite-amplitude resonant oscillations in an enclosure, J. Acoust. Soc. Am. **116**, 2822 (2004).
[46] P. B. Muller, R. Barnkob, M. J. H. Jensen, and H. Bruus, A numerical study of microparticle acoustophoresis driven by acoustic radiation forces and streaming-induced drag forces, Lab Chip **12**, 4617 (2012).
[47] P. B. Muller, M. Rossi, A. G. Marin, R. Barnkob, P. Augustsson, T. Laurell, C. J. Kahler, and H. Bruus, Ultrasound-induced acoustophoretic motion of microparticles in three dimensions, Phys. Rev. E **88**, 023006 (2013).

[48] J. Lei, M. Hill, and P. Glynne-Jones, Numerical simulation of 3D boundary-driven acoustic streaming in microfluidic devices, Lab Chip **14**, 532 (2014).

[49] J. Lei, P. Glynne-Jones, and M. Hill, Acoustic streaming in the transducer plane in ultrasonic particle manipulation devices, Lab Chip **13**, 2133 (2013).

[50] J. J. Lei, P. Glynne-Jones, and M. Hill, Modal Rayleigh-like streaming in layered acoustofluidic devices, Phys. Fluids **28**, 012004 (2016).

[51] F. J. Fahy, *Sound Intensity*, 2nd ed. (E & FN Spon, London, 1995).

[52] mpiv-MATLAB PIV Toolbox, http://www.oceanwave.jp/softwares/mpiv/.

[53] See the Supplemental Material at http://link.aps.org/supplemental/10.1103/PhysRevApplied.8.014018 for the experimental method, numerical method, derivation of active intensities, and additional streaming patterns.

[54] COMSOL Multiphysics 4.4, http://www.comsol.com/.

[55] J. Lei, Formation of inverse Chladni patterns in liquids at microscale: Roles of acoustic radiation and streaming-induced drag forces, Microfluid. Nanofluid. **21**, 50 (2017).

[56] J. A. Mann, J. Tichy, and A. J. Romano, Instantaneous and time-averaged energy-transfer in acoustic fields, J. Acoust. Soc. Am. **82**, 17 (1987).

[57] R. V. Waterhouse, D. G. Crighton, and J. E. Ffowcs-Williams, A criterion for an energy vortex in a sound field, J. Acoust. Soc. Am. **81**, 1323 (1987).

[58] Z. Y. Hong, J. Zhang, and B. W. Drinkwater, Observation of Orbital Angular Momentum Transfer from Bessel-Shaped Acoustic Vortices to Diphasic Liquid-Microparticle Mixtures, Phys. Rev. Lett. **114**, 214301 (2015).

[59] A. R. Rezk, O. Manor, L. Y. Yeo, and J. R. Friend, Double flow reversal in thin liquid films driven by megahertz-order surface vibration, Proc. R. Soc. A **470**, 20130765 (2014).

[60] DOI: 10.5258/SOTON/D0119.